A systematic study of CO₂ planetary atmospheres and their link to the stellar environment

A. Petralia [ID],[1][*] E. Alei [ID],[2][†] G. Aresu,[3] D. Locci,[1] C. Cecchi-Pestellini,[1] G. Micela,[1] R. Claudi[2] and A. Ciaravella[1]

[1]*INAF - Osservatorio Astronomico di Palermo, P.za Parlamento 1, I-90134 Palermo, Italy*
[2]*INAF - Osservatorio Astronomico di Padova, Vicolo dell'Osservatorio 5, I-35122 Padova, Italy*
[3]*INAF - Osservatorio Astronomico di Cagliari, Via della Scienza 5, I-09047 Selargius, Italy*

ABSTRACT

The Milky Way Galaxy is literally teeming with exoplanets; thousands of planets have been discovered, with thousands more planet candidates identified. Terrestrial-like planets are quite common around other stars, and are expected to be detected in large numbers in the future. Such planets are the primary targets in the search for potentially habitable conditions outside the Solar system. Determining the atmospheric composition of exoplanets is mandatory to understand their origin and evolution, as atmospheric processes play crucial roles in many aspects of planetary architecture. In this work we construct and exploit a 1D radiative transfer model based on the discrete-ordinates method in plane-parallel geometry. Radiative results are linked to a convective flux that redistributes energy at any altitude producing atmospheric profiles in radiative–convective equilibrium. The model has been applied to a large number (6250) of closely dry synthetic CO₂ atmospheres, and the resulting pressure and thermal profiles have been interpreted in terms of parameter variability. Although less accurate than 3D general circulation models, not properly accounting for e.g. clouds and atmospheric and ocean dynamics, 1D descriptions are computationally inexpensive and retain significant value by allowing multidimensional parameter sweeps with relative ease.

Key words: radiative transfer – methods: numerical – planets and satellites: atmospheres.

1 INTRODUCTION

The past two decades have seen a major improvement in our knowledge of exoplanet properties, revealing an astonishing diversity in planetary masses, radii, mean temperatures, orbital parameters, and host stellar characteristics and influence. In particular rocky, terrestrial exoplanets such as the one orbiting around Proxima Centauri (Anglada-Escudé et al. 2016) are found at an ever growing rate. It is estimated that approximately 30 per cent of stars in the solar neighbourhood have planets with sizes within two times the Earth's radius and orbital periods within 85 d (Fressin et al. 2013). Around M stars radial velocity surveys provide results even more remarkable: the occurrence of super-Earths in the habitable zone of these stars is about 40 per cent (Bonfils et al. 2013; Kopparapu et al. 2013; Mayor, Lovis & Santos 2014). Thus, small planets orbiting small and cold stars seem to be quite ubiquitous within the Galaxy (Howard 2013).

An important issue is the potential habitability of terrestrial planets orbiting low-mass stars and cool dwarfs. Low-mass stars offer the opportunity for detecting and characterizing habitable terrestrial planets in the next decade. The conventional definition of habitable zone of a planet is usually limited to surface habitability, and the range of orbital distances within which suitable planets can maintain liquid water on their surfaces. Staying in the habitable zone does not clearly constitute a sufficient condition for a planet to preserve liquid water on its surface for geological times. Thus, the habitability of a planet relies on a complex array of geophysical and astrophysical factors.

There is an extensive body of literature on the potential habitability of terrestrial planets in the habitable zone, using both 1D and 3D circulation models, based on Radiative Transfer (RT) platforms simulating synchronous and slow (e.g. Kopparapu et al. 2016), and fast rotating (e.g. Wolf & Toon 2015) planets. The difficulty of assessing the habitability of a planet in alien environments depends mostly on the reliability of simulations in reproducing inherently 3D processes, having only a rough estimate of the planet's past irradiation, and orbital history. 1D models are less performing than 3D simulations in capturing the mean vertical structure of planetary atmospheres, in particular in the case of terrestrial planets in the habitable zone of low-mass stars, and are generally less sensitive than higher dimensional models. Nevertheless, they are very useful to test the effects of some processes, or to explore a parameter space too broad for heavy 3D modelling, such as e.g. the impact of differences in the water vapour content (even in clear-sky conditions) on the inner edge of the habitability zone (Yang, Leconte & Wolf 2016). In other studies, 1D models are used to study the validity of k−distribution when the stellar spectrum is correlated with the atmospheric absorption (H₂O also shapes the spectrum of cool stars), the effect of different collision-induced absorption parametrizations, foreign broadening (i.e. broadening induced by collision with molecules of other species), and various isotopologue

[*] E-mail: antonino.petralia@inaf.it
[†] ETH Zürich, Institute for Particle Physics and Astrophysics, Wolfgang-Pauli-Str. 27, CH-8093 Zürich, Switzerland

ratios. In general 1D models rely just on a few assumptions, and can be easily exploited in a large parameter space, being thus effective in characterizing extrasolar planets.

The minimal set of observables to be derived by modelling efforts are pressure and temperature profiles, abundances and chemistry, and atmospheric dynamics. Even in such limited configuration, the model complexity must increase considerably, if models should reasonably represent the real world. For rocky planets the number of unknowns goes up because of uncertain initial conditions, the interactions between the surface, the interior and the atmosphere, and the possible impact of biological processes. In the simple case of 1D models, one possibility is to consider the energy balance along single air vertical columns, as implemented e.g. in Radiative-Convective (RC) models, in which the only dimension is the altitude.

The introduction of RC models in the 1960s was pioneering for understanding some of the first-order details of planetary climate and climate change (e.g. Manabe & Wetherald 1967). More recently, such models have been exploited to investigate exoplanet habitability either e.g. defining a general habitable zone for N₂/CO₂/H₂O planets (Kasting, Whitmire & Reynolds 1993; Kopparapu et al. 2013), or focusing to single planets (e.g. Gliese 581d; von Paris et al. 2010; Wordsworth et al. 2010; Hu & Ding 2011). This class of models assumes that the vertical structure of an atmosphere is determined by the convection and radiation within the simulated atmospheric column. RC solutions to temperature profiles are computed numerically, frequently using the so-called convective adjustment. This last technique consists in simulating the effects of dry and/or moist convection by adjusting the lapse rate of temperature (and moisture) to specified profiles along the local atmospheric column. The lapse rate (either dry or moist) stabilizes the statistically unstable temperature profile derived from the radiative equilibrium in the deep layers of an atmosphere. Since the vertical temperature gradient changes the energy fluxes, the process must be iterated until the temperature and upwelling flux are continuous (see e.g. Manabe & Strickler 1964). There is no explicit atmospheric circulation, although it is present implicitly, through flux redistribution. RC models may provide useful general indications of the impact on the planetary surface temperature of parameters such as surface pressure and CO₂ mixing ratio.

Exploiting an RC model, we construct a large ensemble of 1D simulations (6250) that systematically vary every relevant external parameter to represent possible exoplanet atmospheres, as we can reliably compute atmospheric profiles in a relatively short time. We want to relate variations in vertical profiles and other atmospheric characteristics (such as e.g. the surface temperature) to chemical trends in the major constituents of the atmospheric gas, and investigate how these relations change with the incoming stellar radiation. These models are useful even if they do not correspond closely to reality, because they allow to confine strange and unfamiliar aspects of atmospheric processes. In Section 2 we briefly describe the physical processes considered and the techniques used in our atmospheric model. The model is validated in Section 3. In Section 4 we confine the parameter space, and show the results. Last section contains our conclusions.

2 THE MODEL

The atmosphere is in hydrostatic balance, and divided into $\mathcal{N}_L$ layers, based on pressure differences. The model consists conceptually of two steps. First, we solve the radiative transfer problem to generates a net radiative flux throughout the atmosphere, taking into account absorption, scattering, and thermal emission, i.e. re-processing of the

incoming stellar radiation. Simple radiative equilibrium gives results that are gravitationally unstable near the surface, and convection must take place to transport heat upwards, reducing the rate at which the temperature in the atmosphere decreases (temperature lapse rate). The second step consists, therefore, in a convective flux that redistributes energy at any altitude.

2.1 The radiative transfer problem

In the solution to the RT problem, we describe the incident stellar flux as a Planck function at the effective temperature of the star, and consider the planetary surface to be Lambertian, i.e. having a grey isotropic reflectivity, R_S. We consider clear sky conditions throughout the atmosphere. We do not also include emission from the top of the atmosphere (TOA), ignoring the existence of a layer of absorbing and re-emitting material.

We generate line-by-line absorption coefficients, and subsequently transform them through a *k*-distribution technique creating look up tables for the absorption coefficients of these species. To minimize the impact of interpolation errors in the radiative fluxes we precalculate the absorption coefficients also accounting for different CO₂ mixing ratios. The line-by-line absorption coefficient is built as follows:

$$
\begin{aligned}
k_\nu &= k_{CO_2} + k_{H_2O} + k_{N_2} \\
&= \omega_{CO_2}\left[\sum_{\delta_{\nu_0}<25\,cm^{-1}} k_\nu^{CO_2} + (1-\omega_{CO_2})\left(\frac{p}{p_{ref}}\right)\left(\frac{T_{ref}}{T}\right)k_f^{CO_2} \right. \\
&\quad \left. + k_\nu^\star \right] + \omega_{H_2O}\left[\sum_{\delta_{\nu_0}<25\,cm^{-1}} k_\nu^{H_2O} + (1-\omega_{H_2O})\left(\frac{p}{p_{ref}}\right) \right. \\
&\quad \left. \times \left(\frac{T_{ref}}{T}\right)k_f^{H_2O} + \omega_{H_2O}\left(\frac{p}{p_{ref}}\right)\left(\frac{T_{ref}}{T}\right)k_s^{H_2O} \right] \\
&\quad + \omega_{N_2}\sum_{\delta_{\nu_0}<25\,cm^{-1}} k_\nu^{N_2},
\end{aligned}
\tag{1}
$$

where ω_i is the Volume Mixing Ratio (VMR) of the *i*-th species, and $\delta_{\nu_0} = |\nu - \nu_0|$; $k_\nu^\star$ indicates the CO₂ self-collision induced absorption, and *f* and *s* stand for foreign- and self-continuum, respectively. We exploit the HITRAN2016 Molecular Spectroscopic Data base (Gordon et al. 2017) in the interval 0.24–1000 μm (10–42 000 cm⁻¹). The line shapes are Voigt profiles, opportunely modified for H₂O and CO₂ (see the Appendix).

Following Mischna, Lee & Richardson (2012) we divide the wavelength range 0.24–1000 μm in 14 bands. Each band is then further partitioned in 10 sub-bands, obtaining a total of 140 bands, and this is the spacing where we apply the *k*-distribution technique. The externally stored *k*-distributed values are defined in Table 1 and they are read and interpolated, according to the required values.

The *k*-distributed transmission is condensed in a few tens of points (i.e. 32) for each band, making the storage of absorption coefficients and their use for the RT calculation fast and simple. A second fundamental benefit of this method is that absorption coefficients at largely different temperature and pressure are now degraded at the same resolution, still maintaining the precise information on the value of the transmission. Since *k*-distributed transmissions are smooth, the RT problem is solved through Gaussian quadrature in each atmospheric layer from the TOA to the surface.

The scattering coefficients are calculated in the Rayleigh approximation as average of coefficients obtained for each molecular specie

Table 1. Opacity table.

Parameter	Values
Pressure (bar)	$10^{-4}, 10^{-3}, 2.5 \times 10^{-3}, 10^{-2}, 2.5 \times 10^{-2}, 10^{-1}, 2.5 \times 10^{-1}, 1, 10, 10^2$
Temperature (K)	100, 150, 200, 250, 300, 350, 400, 450, 500
ω_{CO_2} and ω_{H_2O}	$10^{-6}, 10^{-5}, 10^{-4}, 10^{-3}, 10^{-2}, 10^{-1}, 9.5 \times 10^{-1}$

using the VMRs as weights

$$k(\lambda) = 4.577 \times 10^{-21} \left(\frac{6 + 3D}{6 - 7D} \right) \frac{r^2}{\lambda^4}, \tag{2}$$

where the numerical prefactor is taken from Allen (1973), and the parameters D and r are the depolarization ratio and the refractivity, respectively. The numerical values of these last quantities are taken from the compilation of Vardavas & Taylor (2007, and references therein) in the case of molecular nitrogen and carbon dioxide; for water we use the prescriptions given in von Paris et al. (2010).

The optical depths, obtained by considering both absorption and scattering, are given in input to the DISORT 4 module, the latest version of the DISORT (DIScrete Ordinate Radiative Transfer) software tool (see Stamnes et al. 1988, for its first release), which solves the 1D RT problem by means of the discrete ordinate technique. We use eight streams. Once the RT has been solved in each of the quadrature intervals, the flux in the layers is reconstructed using the same quadrature weights.

The temperature profile in the atmosphere is updated as follows:

$$T_n = T_{n-1} + \frac{dT}{dt} \Delta t = T_{n-1} + \frac{g_P}{c_P} \frac{\Delta F}{\Delta P} \Delta t, \tag{3}$$

where T_{n-1} and T_n are the temperature at the $(n-1)$-th and n-th time-steps, g_P the planetary gravitational acceleration, c_P the specific heat at fixed pressure of the atmospheric gas mixture, and ΔF and ΔP net flux and pressure differences between the top and the bottom of each atmospheric layer, respectively. The time-step is chosen as the minimum between 16 h and the one that would give a maximum temperature variation $\delta T = (g_P/c_P) \times (\Delta F/\Delta P)\Delta t = 4K$.

2.2 Convective adjustment

We simulate the convective redistribution of energy through convective adjustment, a procedure based on local mixing within unstable layers: whenever the radiative equilibrium lapse rate exceeds some pre-specified value marking the passage from the radiative to the convective regime (critical lapse rate, CLR), upward heat transport occurs to restore the lapse rate to that pre-specified value, while conserving the mean energy of the two layers (Manabe & Wetherald 1967). We use either constant and altitude-dependent CLRs. In this latter case we exploit the following weighted expression for the CLR in a non-saturated atmosphere

$$\Gamma_c = -\left(\frac{dT}{dz} \right)_c = (1 - \phi)\Gamma_d + \phi\Gamma_w, \tag{4}$$

where z is the altitude, $\phi(z)$ being the relative humidity, and

$$\Gamma_w = \Gamma_d \times \left(\frac{1 + \omega_s L/\mathcal{R}_d T}{1 + \omega_s L^2/c_P \mathcal{R}_v T^2} \right) \tag{5}$$

is the wet CLR in the adiabatic regime (North & Erukhimova 2009). In equation (5), Γ_d is the dry CLR in which we include CO_2 condensation when required. Its value in the non-condensing regime is given by $\Gamma_d = g_P/c_p$. We use the same formalism as for water, with the exception of directly comparing pressures instead of defining a

humidity. In the above expressions for the CLRs, equations (4) and (5), L is the specific enthalpy of vapourization, ω_s the saturation vapour mixing ratio (the ratio between the mass of saturated vapour and the mass of dry air), and $\mathcal{R}_d$ and $\mathcal{R}_v$ the specific gas constants for dry air and vapour, respectively. We assume an initial isothermal profile at the atmospheric temperature of a leaky greenhouse model $T_s = [1/(2 - \epsilon)]^{1/4} T_{eq}$, where ϵ is the emissivity parameter at the TOA and

$$T_{eq} = T_\star (1 - A)^{1/4} \sqrt{\frac{R_\star}{2d_P}} = \left(\frac{1 - A}{4} \times \frac{S_\star}{\sigma} \right)^{1/4} \tag{6}$$

the equilibrium temperature of the planet. In equation (6) $T_\star$ is the stellar temperature, $R_\star$ the star radius for a main-sequence star (Cox 2000), A the planetary albedo, $S_\star$ the incident stellar flux at TOA, σ the Stefan–Boltzmann constant, and

$$d_P = R_\star \sqrt{\frac{\sigma T_\star^4}{S_\star}} \tag{7}$$

the orbital distance. In the determination of the initial temperature we set $A = 0$ in addition to $\epsilon = 0$.

In the case of wet atmospheres, we compute the initial water vapour pressure as $P_w = \phi(z) \times P_{sat}$, where P_{sat} is the saturation pressure. The humidity profile is $\phi(z) = 1.02 \, \phi_{surf} \times (\mathcal{Q}(z) - 0.02)$ (Manabe & Wetherald 1967), where the factor $\mathcal{Q}(z)$ is the ratio between the initial pressure of the layer, $P(z)$ and the initial surface pressure P_{surf}, and ϕ_{surf} is the humidity at the surface. The minimum allowed value of this quantity is $\mathcal{Q} = 0.02$, and we forced any lower value to such limit, resulting in dry layers at low pressures (i.e. low $\mathcal{Q}$). Depending on the local temperature, the partial pressure of water is calculated at each iterative step, and thus the total pressure.

3 VALIDATING THE CODE

3.1 RT validation

We consider an hypothetical early Mars atmosphere distributed in $\mathcal{N}_L = 100$ layers predominantly of CO_2 composition (95 per cent) with a surface pressure $P_{surf} = 500$ mbar. Temperature and water VMR profiles are taken from Mischna et al. (2012). The temperature rises rather linearly from a surface temperature $T_{surf} = 250$ K to ~ 170 K at a pressure of 100 mbar, and then it is let constant. The same occurs for water vapour whose atmospheric distribution follows closely the temperature profile. At the surface $\omega_{H_2O} = 1.5 \times 10^{-3}$, and it decreases upwards to $\omega_{H_2O} = 10^{-7}$ at 100 mbar, where it remains constant for lower pressures. The remaining ~ 5 per cent atmospheric gas is N_2. To compare our results with others obtained using similar models we call the portion of spectrum between 0.24 and 4.6 μm solar, while the remaining part extending to the far-infrared IR. This separation is artificial, and it does not play any role in the RT solution. It will not be used elsewhere in this work.

We set the surface reflectivity $R_S = 0$, and we consider an irradiation perpendicular to the horizontal plane, i.e. $\cos(\varphi) = 1$, φ being the irradiation Solar (Stellar) Zenith Angle (SZA). In this
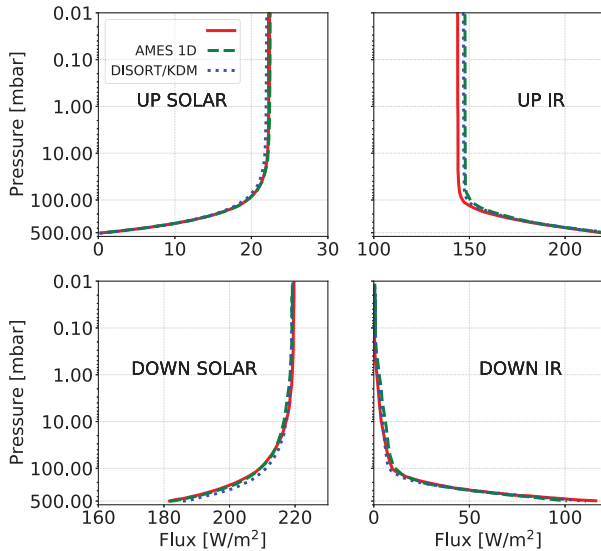
Figure 1. Upward and downward fluxes in the solar and IR bands. Our RT model: red solid lines; NASA Ames model: green dashed lines; Mischna et al. (2012) absorption coefficients incorporated in our RT code: blue dotted lines.

Table 2. Calculation parameters for the present-day Mars simulation.

Parameter		Value
Stellar irradiation	$S_\star$ (Wm^{-2})	586
Stellar temperature	$T_\star$ (K)	5778
Stellar radius	$R_\star$ ($R_\odot$)	1.0
Orbital distance	d_P (AU)	1.523
Planet mass	M_P ($M_\oplus$)	0.107
Planet radius	R_P ($R_\oplus$)	0.531
Zenith angle	φ (degrees)	20,45
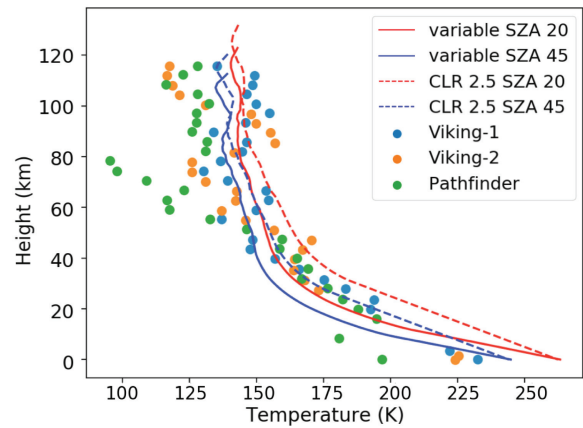
Figure 2. Synthetic (solid and dashed lines) and retrieved (dots) thermal profile of Mars. Red ($\varphi = 20°$) and blue ($\varphi = 45°$) lines: solid, variable CLR from equation (5); dashed, constant CLR, $\Gamma_c = 2.5$ K km^{-1}. Blue dots: *Viking-1*; orange dots: *Viking-2*; green dots: *Pathfinder*. Data from *Viking-1* and *Viking-2* are taken in Nier et al. (1976), while the ones from *Pathfinder* in Magalhães, Schofield & Seiff (1999).

section we do not include CO$_2$ condensation in the model, not even as a simple correction to the $P - T$ profile (e.g. Hu & Ding 2011; Ozak, Aharonson & Halevy 2016).

In Fig. 1 we plot the upward and downward fluxes in the solar and IR bands. We set the solar radiation intensity equal to 220 W m^{-2}, which is approximately the expected illumination for a young Mars ($\sim$75 per cent of the current solar intensity). This value also includes a factor 0.5 for slowly rotating planets. To validate our code we compare the present results with those obtained using a similar 1D *k*-distribution RT model developed at NASA Ames (Toon et al. 1989). We also incorporate the absorption coefficients calculated from Mischna et al. (2012) into our RT module, and show the resulting outcomes in the figure. The different cross-sections and the different RT module do not introduce important differences in the downward fluxes, while there is $\sim$2.5 W m^{-2} difference in the upward solar flux, where Rayleigh scattering dominates. This is a straightforward consequence of the different resolutions at which calculations are performed by the different models. Contrary to our model, in both NASA Ames and Mischna et al. (2012) model opacities the Rayleigh scattering cross-section in a given spectral range is calculated at the centre of the band. Because the Rayleigh scattering depends steeply on wavelengths, low-resolution calculations tend to underestimate the cross-sections.

3.2 Testing the RC model

Once validated the RT model, we apply the integrated model (RT + RC descriptions) to a present-day Mars-like, synthetic atmosphere. The gas is predominantly composed by CO$_2$ (95 per cent) with a mean surface pressure $P_{surf} = 6.72$ mbar. N$_2$ fills the remaining 5 per cent of the atmospheric gas. We assume a completely dry atmosphere. The parameters describing the relevant conditions in the atmosphere, and the boundary conditions are reported in Table 2.

We start from an initial isothermal profile at the temperature $T(z) = T_s = 180$ K. Using an SZA $\varphi = 45°$ (approximately the *Viking-2* landing site latitude), we find results consistent with data acquired during the descent of some of the major martian landers for a constant CLR, $\Gamma_c = 2.5$ K km^{-1} (see Fig. 2). This value is significantly lower

than the dry adiabatic lapse rate, due to heating caused by suspended dust particle absorption, as well as circulation phenomena. The $P - T$ profile obtained using a variable with altitude CLR, computed through equation (5) is also shown. The surface temperatures differ of a few degrees. The atmosphere is globally colder when using the variable CLR.

In Fig. 2 are also shown two additional profiles, both of them derived using an SZA $\varphi = 20°$, similar to *Pathfinder* and *Viking-1* landing sites' latitudes. The illumination angle plays an important role, e.g. in determining the surface temperature (around 20 K difference). The case in which the CLR is derived through equation (5), $\Gamma_c \sim 5$ produces a $P - T$ profile close to the one obtained using a constant CLR, $\Gamma_c = 2.5$ K km^{-1} and SZA, $\varphi = 45°$, although deviates significantly from this latter close to the surface, favouring a much warmer surface temperature, $\sim$265 K. The evolution of the CLR is shown in Fig. 3. In the convection-dominated zone we obtain $\Gamma_c \lesssim 5$.

4 RESULTS

We have constructed a grid of 6250 models of dry planetary atmospheres considering a range of possible stellar and planetary parameters (see Table 3). For all models, the SZA is $\varphi = 60°$, the emissivity parameter at TOA $\epsilon = 0$, and the surface reflectivity $R_S = 0.3$. A point grid in our parameter space is defined by two stellar characteristics, effective temperature ($T_\star$) and incident flux at TOA ($S_\star$), and three planetary features, gravity (g_P), surface pressure (P_{surf}) and CO$_2$ VMR (ω_{CO_2}). Among the outputs, there are the emergent
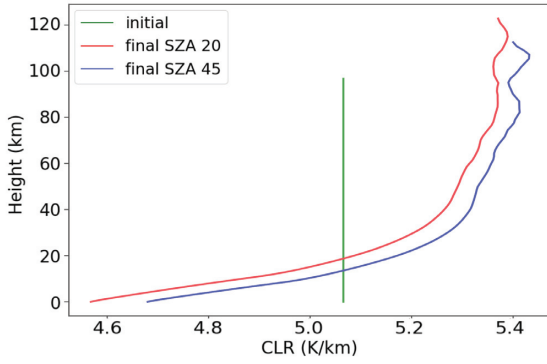
Figure 3. CLR as a function of the altitude. Initial value: green vertical line; final profiles: $\varphi = 20°$, red line; $\varphi = 45°$, blue line.

Table 3. Input parameters considered for the computation of the atmospheric grid.

Parameter	models	Values
$S_\star$ at TOA (Wm^{-2})	5	$\Delta S_\star = 270, 120 - 1200$
$T_\star$ (K)	5	$\Delta T_\star = 1000, 3000 - 7000$
g_P (m s^{-2})	5	$\Delta g_P = 11.25, 5 - 50$
P_{surf} (bar)	10	$\log_{10}(\Delta P/\text{bar}) = \sim 0.22, 0.3 - 30$
ω_{CO_2}	5	$0.0001, 0.01, 0.1, 0.5, 0.9$

spectrum, either the planet–star flux ratio or the planet flux alone, and pressure–temperature $P - T$ profiles.

In the light of the huge number of products, we deal with the general properties of derived synthetic atmospheres, such as e.g. the conditions for gas condensation, the relation of the planetary albedo with the stellar temperature and illumination, and the connection between surface temperature and orbital distance, stellar temperature, and stellar irradiation.

Among the explored models, in a few cases gas temperatures are, at least in one layer, beyond the temperature range of our opacity table (see Table 1). These models are tagged as *crashed*, and included only in the characterization of CO_2 condensation for statistic purposes.

4.1 CO₂ condensation

In Fig. 4, we present the distribution of parameters against the number of both condensing (~ 1000) and non-condensing (~ 5000) models. In the figure we also show the effect of including crashed (~ 250) models and the ratio of condensing and non-condensing models. Since upon convergence such models might end up either condensing and non-condensing CO_2, we add them to both classes of models.

Looking at the scatter in the parameter distributions, it is clear that not all of them play equivalent roles in characterizing the condensation process, with stellar parameters being (relatively) more influential than planetary ones. The number of condensing models dramatically decreases with increasing incident stellar flux: atmosphere with high illumination gets hotter than the lower flux counterpart, thus exhibiting higher saturation pressures of CO_2. Most of the condensing models occur under an irradiation $S_\star \lesssim 400 \, \text{Wm}^{-2}$. For similar considerations the number of condensing models increases together with the stellar temperature: atmospheres illuminated by cold stars absorb more radiation and get hotter than atmospheres of planets orbiting hotter stars.

The condensation occurrence is largely insensitive to surface pressure, as long as we do not consider crashed models. Low

gravity models tend to prevent condensation, although in general non-condensing models are evenly distributed among all the assumed values of surface gravity, pointing out the scarce importance of this parameter. This is particularly evident if we ascribe crashed models to the non-condensing atmosphere set. The CO_2 mixing ratio exhibits wider variations in condensing cases because CO_2 partial pressure is evidently related to condensation.

Finally, in Fig. 4 (bottom right-hand panel) we show a typical $P - T$ profile for a condensing model. Anytime at a location z in the atmosphere (with local P_z and T_z), the CO_2 partial pressure $P_{CO_2}(z)$ exceeds the local vapour saturation pressure $P^{sat}_{CO_2}(T_z)$ we set $P_{CO_2}(z) = P^{sat}_{CO_2}(T_z)$. In other words, we implicitly suppose that latent heat released by CO_2 condensation warms the layer where condensation occurs, and alters the local thermal profile.

4.2 Albedo

In Fig. 5 we present the modelled planetary albedo obtained by the ratio between outgoing and incoming solar radiation fluxes. The albedo ranges from 0.2 to 0.7, with the majority of models (~ 4500) lying in the range $0.2 - 0.4$, a value close to the reflectivity of the surface. In a smaller fraction of models (~ 1500) the albedo ranges over 0.4. The albedo depends strongly on the stellar temperature because of the wavelength dependence of the Rayleigh scattering, equation (2): possessing a wider infrared spectral distribution, the irradiation from colder stars is less scattered than the radiation emitted from hotter stars. The highest albedo values are obtained for stellar temperatures over 6000 K.

4.3 A guess on habitability

In this section, we use the surface temperature as a proxy for habitability. We don't discuss here what makes an extraterrestrial world habitable (see e.g. Meadows & Barnes 2018). Since the atmospheric pressure affects the liquid water temperature range that is commonly used to define planetary habitability, for the sake of simplicity we term as *habitable* those models in which the surface temperature is between the freezing and boiling points of water. The distributions of surface temperatures obtained for condensing and non-condensing models are different (Fig. 6), with the former confined to the lowest temperatures, peaking at 200 K, while the latter presenting a broader distribution centred at 300 K. Taking into account constraints posed by the phase diagram of water we derive that ~ 3500 models would have liquid water on the surface, and would be, potentially, habitable. Since water is essential to life as we know it, this should be the first step for narrowing down which requirements are needed. On the other hand, this very first bit of information neglects other demands of life, such as e.g. a source of carbon, an energy source, and essential nutrients. Moreover, it could be misleading being too Earth-centric.

The connection between surface temperature and orbital distance, stellar temperature and illumination is presented in Fig. 7. About two-thirds of our modelled planets lie at distances lower than 2 AU, while the remaining ~ 2000 are at farthest locations from their central stars, with some of them having very large orbital distances, up to 12 AU. Given the assumed flux range, we do not include planets orbiting hot stars ($T_\star \gtrsim 6000$ K) at distances lower than 1 AU, while those planets orbiting colder stars ($T_\star \lesssim 4000$ K) are never beyond 2 AU. For orbital distances $d_P \lesssim 1$ AU, in about two-thirds of cases the planets are habitable and orbit around stars whose temperatures are $T_\star \lesssim 5000$ AU. In the second bin, comprising planets orbiting
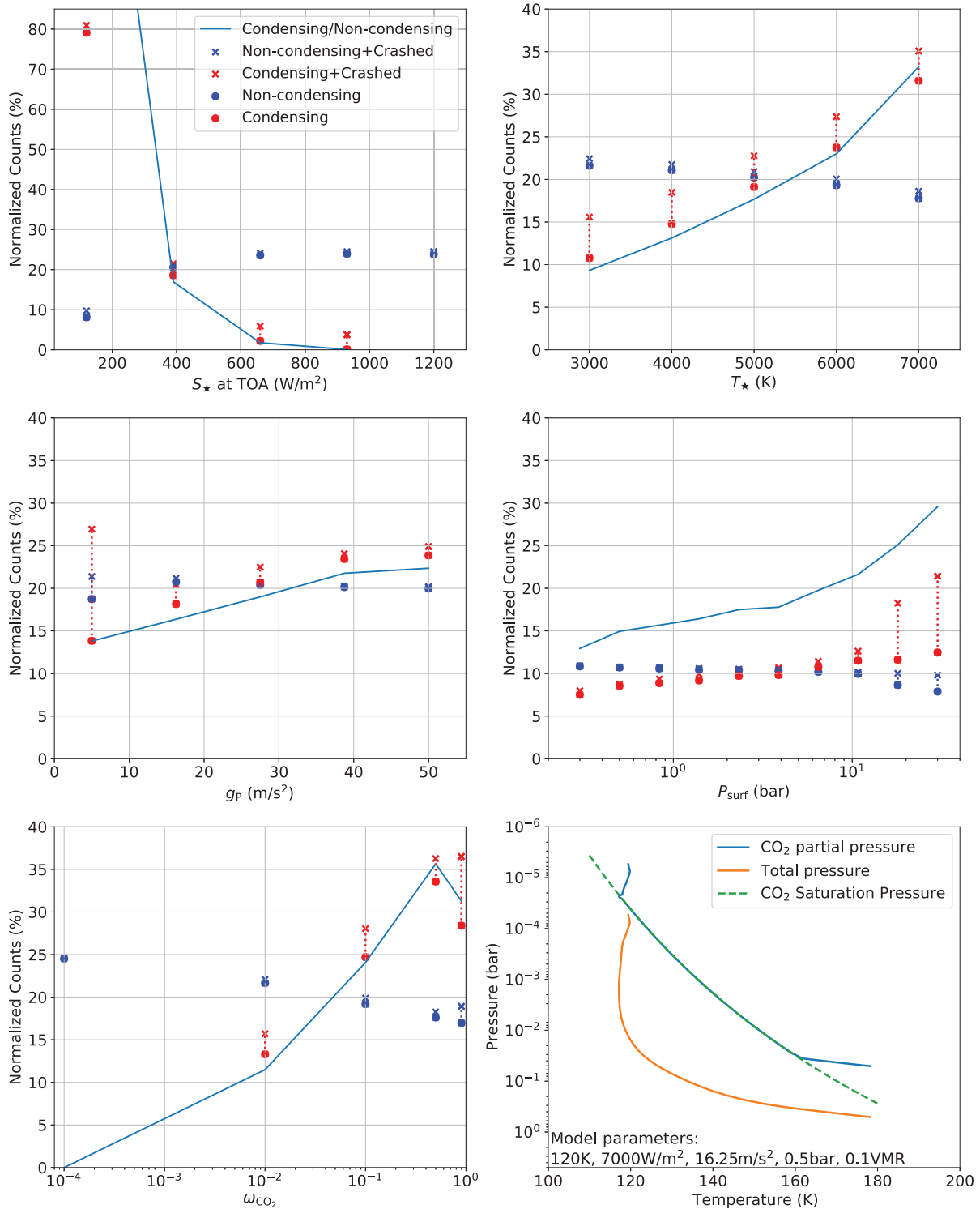
Figure 4. The distribution of model parameters in the case of condensing (red filled circles) and non-condensing (blue filled circles) models. Both classes of models are normalized to their total counts. A dashed line, bounded by crosses, marks the variation introduced by *crashed* models (see the text). The blue line describes the variation in the ratio between the number of condensing and non-condensing models. In the bottom right-hand panel is shown the CO_2 partial pressure profile as a function of temperature for a condensing atmosphere (solid blue line); the green dashed line represents the CO_2 phase diagram, while the orange solid line the total pressure profile; modelling parameters are reported as labels.

between 1 and 2 AU, we get habitable conditions only for stars with $T_\star = 5000$ and 6000 K. The rest of the sample models needs hot stars to be habitable. Farther than $d_P = 6$ AU, there are no more habitable models.

### 4.4 Surface and planetary equilibrium temperatures

In Fig. 8 we present the relation between the modelled surface temperature and the equilibrium temperature, derived using equation (6) in which the albedo is a result of the modelling procedure. We first
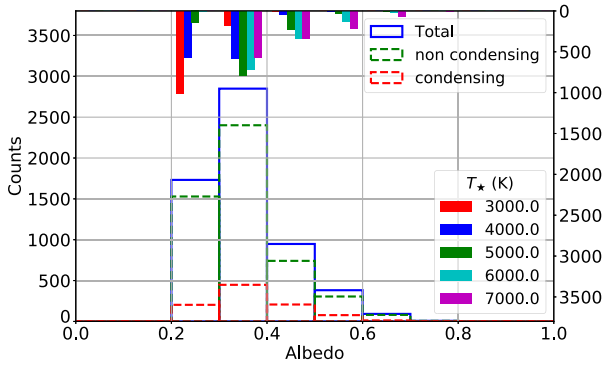
Figure 5. Histogram (counts on the left ordinate axis) of modelled albedos for condensing (red dashed), and non-condensing (green dashed) models; the solid blue line describes the whole set of models. For each albedo bin, the stellar temperature ($T_\star$) distribution is shown as a reversed histogram whose counts are displayed in the right ordinate axis.
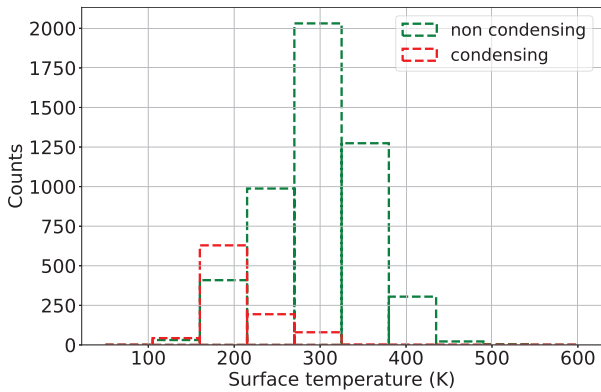
Figure 6. Histogram of modelled surface temperatures for condensing (red dashed), and non-condensing (green dashed) models.
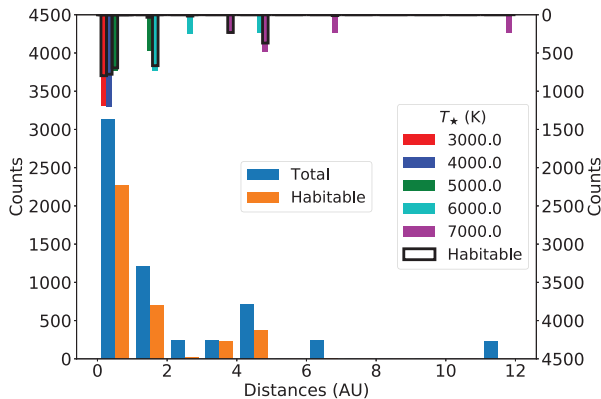
Figure 7. Histogram of modelled distances (left and bottom axis), for the totality of the models (blue), and for the subset of the habitable planets (orange), together with the distribution of the stellar temperatures ($T_\star$, right and top axis). In this latter diagram the black empty boxes mark the fraction of habitable planets.

present the entire set of models (in the top left-hand panel), with each model labelled by the stellar flux incident at the TOA, $S_\star$. In order to understand how the temperatures are related to the input parameters, we extract subsets of data points, defined by selecting, consecutively, specific values of different model parameters, namely the flux at

TOA (top right-hand panel, labelled by stellar temperature, $T_\star$), two stellar temperatures (mid and bottom left-hand panels, labelled by surface pressure, P_{surf}) and two surface pressures (mid and bottom right-hand panels, labelled by gravity, g_P). We also highlight albedo values (mid and bottom right-hand panels) through the sizes of the symbols exploited to flag a model in the temperatures' plane.

By looking at the entire set (top left-hand panel), it is evident that surface temperatures are always greater than the equilibrium temperatures, and both of them increase with the incident flux, as the flux enters directly in the estimation of planetary temperatures. Selecting an intermediate value for the flux, $S_\star = 660\,\mathrm{W\,m^{-2}}$, we may analyse how different parameters shape its dispersion properties and therefore how much the surface temperature differs from the equilibrium temperature. We find that different stellar types have completely different dispersion (top right-hand panel). Cold stars (red circles) provide very similar equilibrium temperatures with a dispersion $\Delta T_{eq} \sim 20\,\mathrm{K}$, while hotter stars (blue circles) show broader temperature distributions increasing with the stellar temperature up to $\sim 50\,\mathrm{K}$. The different equilibrium temperatures between cold and hot stars are primarily due to the very different modelled albedo (see Fig. 5). Planets facing cold stars have a small range of possible albedos close to the reflectivity of the surface ($R_S = 0.3$) while the ones facing hot stars showing a much broader range of albedos (up to 0.7). To understand the dispersion of the surface temperatures, in the last (mid and bottom) panels we show the effects of the surface pressure, gravity and albedo in the models produced using the end points of the assumed stellar temperature distribution, i.e. $T_\star = 3000$ (mid panels) and 7000 K (bottom panels).

In both cases, the dispersion in the surface temperatures increases with the surface pressure from $\Delta T_{surf} \sim 20\,\mathrm{K}$ at 0.3 bar to $\Delta T_{surf} \sim 120\,\mathrm{K}$ at 30 bar. The role of gravity is marginal, and it contributes only partially in hot star environments by lowering the dispersion. The opposite is true for the albedo (cf. the symbol sizes in the two lowest right-hand panels). In general, the highest surface temperatures are reached for large values of the surface pressure. This behaviour is driven by the CO_2 greenhouse effect. As the CO_2 content increases and the atmosphere becomes opaque to outgoing infrared radiation, this determines the maximum greenhouse effect (see Kasting et al. 1993 and Kopparapu et al. 2013). This is evident in the bottom left-hand panel of Fig. 8, where the increase in the surface pressure does not drive anymore the increase in the surface temperature. The influence of the incident stellar spectrum, can be seen in the top right-hand panel where cooler stars show a less efficient Rayleigh scattering, resulting in higher surface temperatures.

5 CONCLUSIONS

The wealth of super-Earth detections suggests that terrestrial planets may be abundant in our Galaxy. A large fraction of the stars are likely to harbour rocky planets, and the available observations suggest a heterogeneity of climates. Such variety depends on the planetary physical characteristics (e.g. stellar illumination, orbit, and size) and the composition of its atmosphere. Among others, radiative transport of stellar and thermal radiation through gas and aerosols is a primary key process in a climate system.

In this work, we construct and exploit a 1D RT code based on the discrete-ordinates method in plane-parallel geometry. The RT modelling results are linked to a convective flux that redistributes energy at any altitude producing atmospheric profiles in RC equilibrium. Here, we present simulations of dry atmospheres in
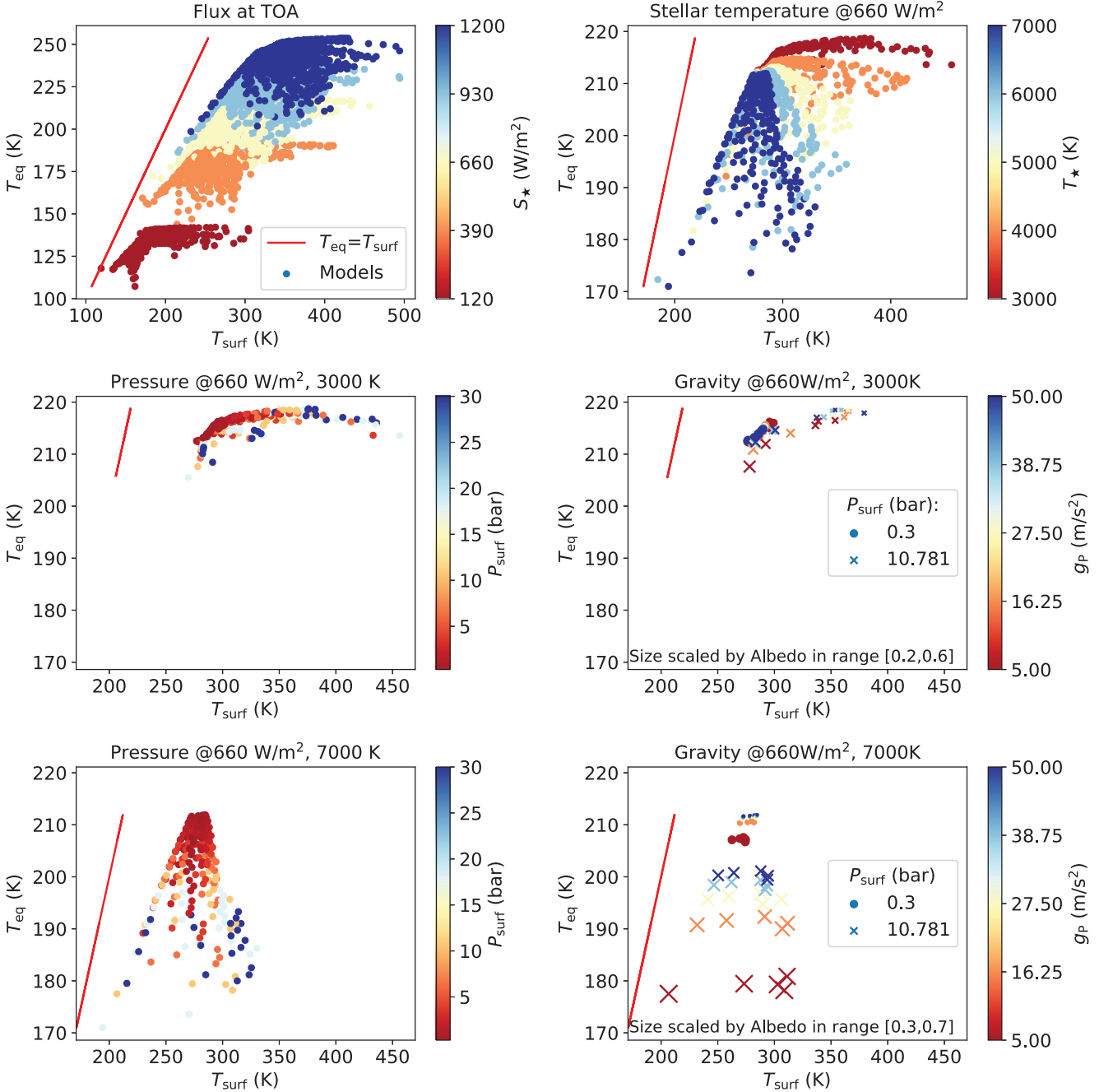
Figure 8. Scatter of modelled surface temperatures, T_{surf} versus the estimated equilibrium temperatures, T_{eq}, computed using equation (6) and the derived albedo. The red line represents the loci defined by the equivalence $T_{eq} = T_{surf}$. Top left-hand panel: the whole set of models labelled by the incident flux, $S_\star$; top right-hand panel: selected models with $S_\star = 660\,\mathrm{W\,m^{-2}}$, labelled by stellar temperature; middle panels: selected models with $S_\star = 660\,\mathrm{W\,m^{-2}}$ and $T_\star = 3000\,\mathrm{K}$, labelled by surface pressure (left-hand panel) and gravity (right-hand panel, for two values of the surface pressure); bottom panels: the same as in middle panels for $T_\star = 7000\,\mathrm{K}$. In the middle and bottom right-hand panels, the sizes of symbols are related to the values of the planetary albedo.

terrestrial-like planets with varying concentration of CO$_2$, around main sequence stars (from M to F types), over a wide range of stellar fluxes and temperatures.

We initially probe the effect of input parameters on the onset of CO$_2$ condensation. As expected, the (average) stellar illumination and CO$_2$ mixing ratio are critical aspects in defining the possibility of condensation. Condensation is suppressed either when the atmosphere receives more than 400 W m^{-2}, and with CO$_2$ mixing ratios

lower than 1 per cent. All other parameters affect the condensation process to a lesser extent.

The modelled albedo is close to the reflectivity of the surface for planets embedded in cold star ($\lesssim 4000\,\mathrm{K}$) environments. The range of the albedo values extends if the planet is located around a hotter star ($\gtrsim 5000\,\mathrm{K}$). Therefore, in the case of our simple atmospheric composition and geometric configuration the albedo acts as a proxy of reflectivity properties of the planetary surface. We recall that we
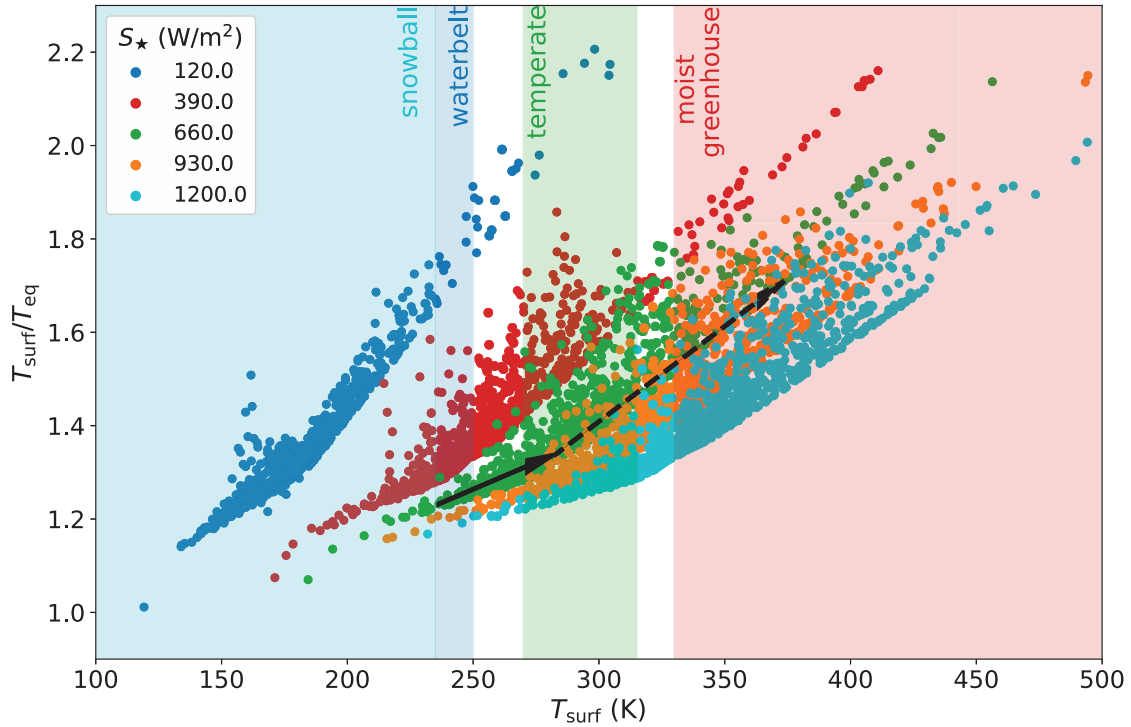
Figure 9. Surface temperatures versus the ratio T_{surf}/T_{eq}. Colours indicate different levels of incident stellar flux. Two arrows mark temperature variations obtained by varying, the stellar temperature (solid black) and the CO_2 mixing ratio (dashed black), setting all the other parameters to the values $S_\star = 660\,\mathrm{W\,m^{-2}}$, $P_{surf} = 30\,\mathrm{bar}$, $g_P = 50\,\mathrm{m\,s^{-2}}$. The solid line represents $T_\star = 7000 \rightarrow 3000\,\mathrm{K}$, with $\omega_{CO_2} = 1 \times 10^{-4}$, while the dashed line connects the model with $T_\star = 3000\,\mathrm{K}$ and $\omega_{CO_2} = 1 \times 10^{-4}$, to the one with $T_\star = 3000\,\mathrm{K}$ and $\omega_{CO_2} = 0.9$. For illustration only, we show on the background the different climate regimes identified by Wolf et al. (2017).

consider a perfectly Lambertian surface, for which the hemispherical reflectance is simply equal to the reflectance factor independently of viewing geometry.

We also explore the conditions for (a restricted definition of) habitability both in terms of surface temperature to sustain liquid water and orbital distances. We find that more than half of the planets would be habitable, with the majority having orbital distances $\lesssim 2\,\mathrm{AU}$ and a small, but not negligible fraction extending up to 6 AU.

Finally, we compare the equilibrium temperature of the atmosphere with the modelled surface temperature. The equilibrium temperature represents a sort of lower limit to the surface temperatures, with the extent of the deviation between the two temperatures driven by the characteristics of specific models. The equilibrium temperature is generally used to categorize the potential habitability of exoplanets with Earth-like planetary albedo of 0.3 or 0 (e.g. Anglada-Escudé et al. 2016). As a proxy, the equilibrium temperature has a intrinsically poor reliability because albedos can be very different, and surface temperatures typically exceed equilibrium temperatures by the amount of the atmosphere's greenhouse effect. Thus, despite the limited resources, planets should be observed intensely to characterize their atmospheres.

Recently, a few studies typically based on global climate models addressed the problem of the removal of degeneracies arising from relations among observables by estimating albedo, equilibrium temperature, and surface temperature of rocky exoplanets (e.g. Wolf et al. 2017; Del Genio et al. 2019, for a limited manifold of models. Although less accurate, not properly accounting for clouds, sea ice and atmospheric and ocean dynamics, 1D models are computationally inexpensive and allow to expand significantly the explored parameter space. In Fig. 9 we show the ratio T_{surf}/T_{eq} versus

T_{surf} for the whole set of converged models ($\sim$6000). Leaving aside extreme configurations, this relation appears to be roughly linear, with a steepness controlled by the stellar illumination, whose increase tends to moderate the deviation from T_{eq} of surface temperatures. For illustrative purposes only we have shown in the background the four stable climate states defined by Wolf et al. (2017), through mutually exclusive global mean surface temperatures, whose boundaries are separated by abrupt climatic transitions. As an example, we have drawn a path travelled by a data point varying some parameters, while taking fixed $S_\star$ at intermediate illuminations, i.e. $S_\star = 660\,\mathrm{W\,m^{-2}}$. Planets with similar characteristics in surface pressure, $P_{surf} = 30\,\mathrm{bar}$, gravity, $g_P = 50\,\mathrm{m\,s^{-2}}$, and CO_2 VMR $\omega_{CO_2} = 1 \times 10^{-4}$, that are initially in the snowball regime when orbiting hot stars, transit through waterbelt and temperate zones if the stellar temperature decreases to $T_\star = 3000\,\mathrm{K}$. From this location, if the CO_2 VMR increases up to 0.9, our test planet reaches the moist greenhouse state. This simple case illustrates how low dimensional models retain significant value by allowing multidimensional parameter sweeps with relative ease.

In conclusion, we have constructed a horizontally homogeneous model of RC equilibrium to compute the global average of a planetary atmosphere. The model has been applied to a large number of closely dry synthetic atmospheres, and the resulting pressure and thermal profiles have been interpreted in terms of parameter variability. In future works, we shall extend the chemical inventory of the modelled atmospheres, and explore how the relative humidity or cloud distributions are maintained in such idealized systems. Moist convection is dominated by phase changes, and therefore may present peculiar and unfamiliar aspects, that may be usefully isolated in a simple geometry.

REFERENCES

Allen C., 1973, Astrophysical Quantities. The Athlone Press, University of London

Anglada-Escudé G. et al., 2016, Nature, 536, 437

Baranov Y. I., Lafferty W. J., Fraser G. T., 2004, J. Mol. Spec., 228, 432

Bonfils X. et al., 2013, A&A, 549, A109

Cox A. N., 2000, Allen's Astrophysical Quantities. Springer-Verlag, Berlin

Del Genio A. D. et al., 2019, ApJ, 884, 75

Fressin F. et al., 2013, ApJ, 766, 81

Gordon I. E . et al., 2017, J. Quant. Spec. Radiat. Transf., 203, 3

Gruzska M., Borysow A., 1997, Icarus, 129, 172

Halevy I., Pierrehumbert R. T., Schrag D. P., 2009, J. Geophys. Res., 114, D18112

Howard A. W., 2013, Science, 340, 572

Hu Y., Ding F., 2011, A&A, 526, A135

Kasting J. F., Whitmire D. P., Reynolds R. T., 1993, Icarus, 101, 108

Kopparapu R. K . et al., 2013, ApJ, 765, 131

Kopparapu R. K. et al., 2016, ApJ, 819, 1

Kopparapu R. K., Wolf E. T., Arney G., Batalha N. E., Haqq-Misra J., Grimm S. L., Heng K., 2017, ApJ, 845, 5

Magalhães J. A., Schofield J. T., Seiff A., 1999, J. Geophys. Res., 104, 8943

Manabe S., Strickler R. F., 1964, J. Atm. Sci., 21, 361

Manabe S., Wetherald R. T., 1967, J. Atm. Sci., 24, 241

Mayor M., Lovis C., Santos N. C., 2014, Nature, 513, 328

Meadows V. S., Barnes R. K., 2018, in Deeg H., Belmonte J., eds, Handbook of Exoplanets. Springer, Berlin, p. 54

Mischna M. A., Lee C., Richardson M., 2012, J. Geophys. Res., 117, E10009

Mlawer E., Payne V., Moncet J. L., Delamere J., Alvarado M., Tobin D., 2012, Phil. Trans. R. Soc., 370, 2520

Nier A. O., Hanson W. B., Seiff A., McElroy M. B., Spencer N. W., Duckett R. J., Knight T. C. D., Cook W. S., 1976, Science, 193, 786

North G. R., Erukhimova T. L., 2009, Atmospheric Thermodynamics: Elementary Physics and Chemistry. Cambridge Univ. Press, Cambridge

Ozak N., Aharonson O., Halevy I., 2016, J. Geophys. Res. E, 121, 965

Paynter D. J., Ramaswamy V., 2011, J. Geophys. Res. D, 116, D20302

Perrin M. Y., Hartmann J. M., 1989, J. Quant. Spec. Radiat. Transf., 42, 311

Stamnes K., Tsay S.-C., Jayaweera K., Wiscombe W., 1988, Appl. Opt., 27, 2502

Toon O. B., McKay C. P., Ackerman T. P., Santhanam K., 1989, J. Geophys. Res., 94, 16287

van Vleck J. H., Huber D. L., 1977, Rev. Mod. Phys., 49, 939

Vardavas I. M., Taylor F. V., 2007, Radiation and Climate. Oxford Univ. Press

von Paris P. et al., 2010, A&A, 522, A23

Wolf E. T., Toon O. B., 2015, J. Geophys. Res., 120, 5775

Wolf E. T., Shields A. L., Kopparapu R. K., Haqq-Misra J., Toon O. B., 2017, ApJ, 837, 107

Wordsworth R. D., Forget F., Selsis F., Madeleine J.-B., Millour E., Eymet V., 2010, A&A, 522, A22

Yang J., Leconte J., Wolf E. T., 2016, ApJ, 826, 222

APPENDIX A: LINE MODIFICATIONS AND CONTINUUM DESCRIPTION

Carbon dioxide line profiles are observed to be sub-lorentzian away from the line centre. We use the scaling factor suggested by Perrin & Hartmann (1989) beyond $3\,\text{cm}^{-1}$ from the line centre. Moreover, to adjust for the asymmetry of the line profile we applied the normalized correction factor given in van Vleck & Huber (1977). The CO_2 continuum is computed using a semi-empirical model, which provides the foreign continuum from 1 to $1000\,\mu\text{m}$ or 0.1–$10\,000\,\text{cm}^{-1}$ (MT_CKD continuum v2.5.2; Mlawer et al. 2012). The CO_2 molecule also experiences collision induced absorption due to encounters with other CO_2 molecules. We account for these effects using the theoretical results of Gruzska & Borysow (1997) in the interval 33–$1000\,\mu\text{m}$ (10–$300\,\text{cm}^{-1}$) and interpolating the experimental results of Baranov, Lafferty & Fraser (2004) in the interval 5–$9\,\mu\text{m}$ (1100–$2000\,\text{cm}^{-1}$). To avoid an overestimate of the absorption, each CO_2 line is calculated out to $25\,\text{cm}^{-1}$ from the line centre, hence (as suggested by Mlawer et al. 2012) we consider continuum all the absorption produced further.

In the case of H_2O we follow the prescriptions of Halevy, Pierrehumbert & Schrag (2009) and Mischna et al. (2012). We compute a Voigt profile within 40 times the Doppler width from the line centre, and a Van Vleck-Weisskopf profile out to $25\,\text{cm}^{-1}$ from the natural wavenumber of the transition ν_0. Also for water, we use the continuum model given in Mlawer et al. (2012), which provides both foreign and self continuum from 0.5 to $1000\,\mu\text{m}$ (0.1 to $20\,000\,\text{cm}^{-1}$). Such a model derives H_2O line shapes by fitting the continuum in spectral regions where it is best constrained by measurements. The same line shape is extended to spectral regions where the continuum is not well-constrained or simply never been measured.

Recently, Kopparapu et al. (2017) implemented a new water vapour continuum model (Paynter & Ramaswamy 2011), derived from laboratory measurements taken at temperatures appropriate for atmospheres expected near the inner edge of the habitable zone. Such model provides a continuum absorption stronger than in the model put forward by Mlawer et al. (2012). While this is not influential on the results of this work, we shall update the spectroscopic data base in future releases of our model, e.g. testing the recently released 3.3 version of the MT_CKD continuum.

This paper has been typeset from a TEX/LATEX file prepared by the author.